metals

MDPI

Article

Towards a Methodology for Component Design of Metallic AM Parts Subjected to Cyclic Loading

Uwe Zerbst *, Mauro Madia, Giovanni Bruno and Kai Hilgenberg

Bundesanstalt für Materialforschung und -prüfung (BAM), D-12205 Berlin, Germany; mauro.madia@bam.de (M.M.); giovanni.bruno@bam.de (G.B.); Kai.Hilgenberg@bam.de (K.H.)
* Correspondence: uwe.zerbst@bam.de

Abstract: The safe fatigue design of metallic components fabricated by additive manufacturing (AM) is still a largely unsolved problem. This is primarily due to (a) a significant inhomogeneity of the material properties across the component; (b) defects such as porosity and lack of fusion as well as pronounced surface roughness of the as-built components; and (c) residual stresses, which are very often present in the as-built parts and need to be removed by post-fabrication treatments. Such morphological and microstructural features are very different than in conventionally manufactured parts and play a much bigger role in determining the fatigue life. The above problems require specific solutions with respect to the identification of the critical (failure) sites in AM fabricated components. Moreover, the generation of representative test specimens characterized by similar temperature cycles needs to be guaranteed if one wants to reproducibly identify the critical sites and establish fatigue assessment methods taking into account the effect of defects on crack initiation and early propagation. The latter requires fracture mechanics-based approaches which, unlike common methodologies, cover the specific characteristics of so-called short fatigue cracks. This paper provides a discussion of all these aspects with special focus on components manufactured by laser powder bed fusion (L-PBF). It shows how to adapt existing solutions, identifies fields where there are still gaps, and discusses proposals for potential improvement of the damage tolerance design of L-PBF components.

Keywords: fatigue; fracture; defects; L-PBF

check for updates

Citation: Zerbst, U.; Madia, M.; Bruno, G.; Hilgenberg, K. Towards a Methodology for Component Design of Metallic AM Parts Subjected to Cyclic Loading. *Metals* **2021**, *11*, 709. https://doi.org/10.3390/met11050709

Academic Editor: Yadir Torres Hernández

Received: 22 March 2021
Accepted: 21 April 2021
Published: 26 April 2021

Publisher's Note: MDPI stays neutral with regard to jurisdictional claims in published maps and institutional affiliations.

Copyright: © 2021 by the authors. Licensee MDPI, Basel, Switzerland. This article is an open access article distributed under the terms and conditions of the Creative Commons Attribution (CC BY) license (https://creativecommons.org/licenses/by/4.0/).

1. Specific Aspects of Fatigue Assessment of L-PBF Manufactured Materials and Components

Common design philosophies comprise (a) *safe life design* = no failure over the projected lifetime without accompanying measures, (b) *damage tolerant design* = failure during the projected lifetime possible but prevented by accompanying measures, usually repeated inspections, (c) *fail safe design* = the failure of a substructure detected in time to prevent failure of the entire component.

The topic of this paper is *safe life design* as the basic safety option but tailored for AM, specifically laser powder bed fusion (L-PBF) applications. Conventionally, *safe life* is realized by the application of the S–N curve concept. In the case of additive manufacturing, however, this reaches its limits for a number of reasons discussed below:

1.1. The Outstanding Role of Material Defects

Figure 1 shows a commonly used correlation between the hardness (which correlates with the ultimate tensile strength R_m) and the endurance limit σ_e. The curves consist of a straight section that bends downwards above a certain hardness or strength. It is given for different steels. The turning point is material dependent (see [1]).

The mechanism behind this curve shape can be readily explained: In engineering alloys, fatigue cracks initiate at defects. These can be material defects such as non-metallic inclusions, cavities (pores, lack of fusion) or faulty microstructures in areas of designed notches. It can also be a pronounced surface roughness. Furthermore, defects can be the

result of insufficiently careful production or maintenance (e.g., scratches) or may arise during operation (e.g., foreign object damage or corrosion pits). This is discussed in detail in a paper series of the authors [2–4]. At stress levels below the endurance limit, individual microcracks arrest after some propagation. The endurance limit characterizes the transition from crack arrest to continued growth [1,5]. If the crack propagation barrier is overcome due to certain mechanisms, e.g., corrosion or damage accumulation, the endurance limit will also disappear leading finally to failure even by small stress amplitudes.

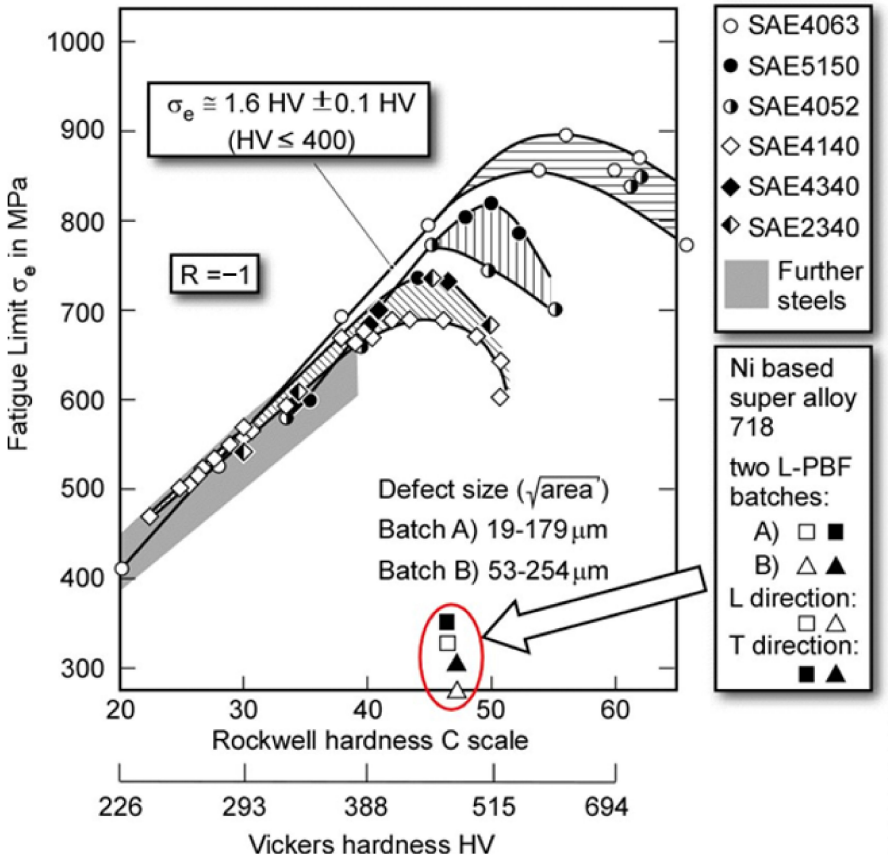


Figure 1. Relationship between the hardness and the fatigue limit of steels [1]. The dots for the L-PBF examples are taken from [6].

It is important that the arrest crack depth depends on the strength of the material. The higher the strength the smaller the arrest crack size, and vice versa. In a theoretical simulation, the authors obtained the arrest depth of an assumed semi-circular surface crack as 19 ± 2 µm for S355NL steel (R_m = 555 MPa) and 11 ± 1 µm for S960QL steel (R_m = 1057 MPa) [7]. This is in line with empirical data indicating critical defect sizes in the order of 10 to 25 µm for steel and aluminum, below which no harmful effect on the endurance limit or an equivalent of this is stated [3,4].

In Figure 1, the straight section describes the range in which the endurance limit is controlled by crack arrest. This is the case for low-strength materials. When hardness and strength are increased, the arrest crack size becomes smaller, and when it falls below the size of the pre-existent defects, no crack arrest occurs any longer. In such a case, the defect size immediately controls the fatigue limit, and the $\sigma_e - HV$ curve bends downwards.

In the case of L-PBF materials, we find that the whole scheme no longer works; see the dots near the X-axis. In fact, the defect size is for L-PBF in the experiments reported in [6] much above the critical value mentioned above (80 µm for batch A and even 149 µm for batch B).

In the context of a similar study, Murakami et al. [8] concluded that the relation $\sigma_w = 1.6\ HV \pm 0.1\ HV$ (resulting values in MPa) of the straight line in Figure 1 up to

$HV \approx 400$ is applicable to additive manufacturing only in combination with hot isostatic pressing (HIP) and surface polishing. The consequence is that, in the general case, defects have always to be taken into account for L-PBF materials.

A brief discussion of the defect types typical for L-PBF is provided in Section 2, and approaches for treating them in component assessment in Section 3.

1.2. Problems in Determining Material Properties

Additive manufacturing technologies such as L-PBF are comparable with welding, but the molten volumes are very small. The consequences are extreme cooling conditions with cooling rates from 10^3 to 10^8 K/s [9]. These have an effect on the resulting microstructure and defect generation. Likewise, reheating when the next layer is exposed also plays a role. There is also energy dissipation in the bulk and support structures. An important parameter is the so-called interlayer time, i.e., the time between two successive layers. It is well known that this has a big influence on heat accumulation and defect formation [10,11] as well as on the deformation properties, particularly on the elongation at fracture; see, e.g., [12]. Zhang et al. [13] propose using this parameter as an indicator for the endurance limit. This makes sense because both parameters are controlled by near-surface defects.

The effect of the technological parameters on the local microstructure and the local defect population on the local material properties is discussed in detail in [14,15]. The point we want to make here is that the complex thermal conditions cause a large-scale heterogeneity of the microstructure. This heterogeneity makes the determination of material parameters for a L-PBF structure a non-trivial task. In fact, one cannot talk any longer about material properties but must take into account their variability along different locations in the structure. In order to meet the requirements, thermally simulated specimens must be tested, contrary to the current practice of testing accompanying specimens experiencing different thermal regimes. This will be the topic of Section 4.

1.3. Damage-Relevant Sites in an L-PBF Component

It is common practice in component assessment not to consider the entire part but to concentrate on the highest loaded site. This is usually defined by the highest stress. Not just the stress peak value but also its profile in the wall thickness direction become important as soon as cracks or fatigue crack propagation come into play. In cases where ligament yielding plays a role, e.g., in low-cycle fatigue, constraints (or local stiffness) are another characteristic feature.

For L-PBF parts, further aspects have to be considered. The most important one is the pronounced dependence of the properties on the build direction. Figure 2 provides the nomenclature for specimen directions. Note that the poorest mechanical properties are usually obtained for vertical (z) and z–x directions. The relation of the building direction with the loading direction strongly affects damage. In a component of more complex geometry, the situation is not as simple as shown in Figure 2 since the principal stress directions change from site to site.

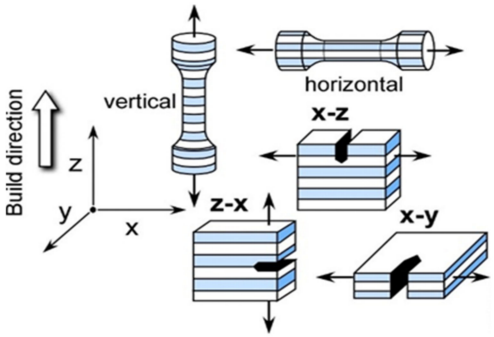


Figure 2. Notation used to relate the loading and crack plane orientation to the build direction in L-PBF.

What is needed, therefore, is a philosophy for the identification of critical sites in components based on mechanical as well as on L-PBF specific features. A proposal is presented in Section 5.

1.4. Residual Stress Pattern

A widely unsolved problem in additive manufacturing is that of residual stress. In structures without cracks, residual stresses (RS) mainly play a role via secondary effects such as distortion [16]. However, in the presence of cracks, RS act as a major loading component. This will always be the case in additively manufactured parts. The problem is particularly confusing as the RS state is influenced by a large number of technological parameters such as heat input and dissipation, building direction, scanning strategy and others (see the reviews in [14,17]). An aggravating effect is that there is usually tensile RS at the surface; this fact is particularly detrimental for the fatigue resistance because fatigue crack initiation tends to occur at the surface (at least in the LCF and HCF regimes). Moreover, strong interplay has been observed between RS, microstructure, and existing defects, and they contribute to the LCF and HCF in different ways (see e.g., [18]). From the point of view of the authors, while first proposals for the treatment of residual stresses in L-PBF have been published (e.g., [19,20]), they are not yet fully mature, and the first choice so far is the elimination of the RS by annealing or other post-fabrication measures. This point will not be discussed in further detail in the present paper.

2. Typical Defects in L-PBF

This section focuses on material defects. These can be divided into (a) gas porosity, (b) lack-of-fusion defects, (c) balling defects and keyhole pores, (d) microcracks, and (e) pronounced surface roughness. Again, a more detailed discussion is provided in [14] so that the explanations here can be limited to a few essential points.

2.1. Gas Porosity

Gas bubbles which, during rapid cooling, do not have enough time to ascend to the surface in the melt pool are entrapped in the material. Gas formation can occur due to excessive laser energy, but gas pores can also pre-exist in the metal powder. The size of such pores is usually <100 mm [21], and their shape is spherical; this corresponds to a stress concentration factor of $K_t \approx 2$, but this value becomes larger in the case of pore clusters.

2.2. Lack-of-Fusion Defects

Lack of fusion means that the powder is not fully melted to deposit a new layer. With respect to fatigue, it is more harmful than gas porosity. Indeed, non-welded areas show a pronounced irregular morphology and are rather elongated. Their stress concentration factor is, therefore, (much) larger than 2. This is the case in vertical specimens (see Figure 2) where the defects are formed between the layers [22–25]. In addition, lack-of-fusion defects are typically larger than gas pores (a defect length of 190 µm was found in [12]). The generation of lack-of-fusion defects is facilitated by either too little laser energy input per volume element or too high energy dissipation in the manufacturing setup.

2.3. Balling Defects and Keyhole Pores

Balling defects are the consequence of poor wetting. This causes the break-up of thin melt pools. Spherical droplets of molten metal with diameters in the order of the laser beam diameter are formed [26]. While the reason for balling can be insufficient energy or too high laser speed, keyhole pores are caused by the opposite, i.e., too high energy density. The deep and narrow melt pool makes it difficult for the pores to escape from it so that they remain entrapped when the keyhole collapses [27].

Figure 3 provides an overview on the formation of the different defect types discussed so far depending on the laser power and the scan speed on the example of L-PBF manufactured Ti–6AL–4V (see [12,23,24]).

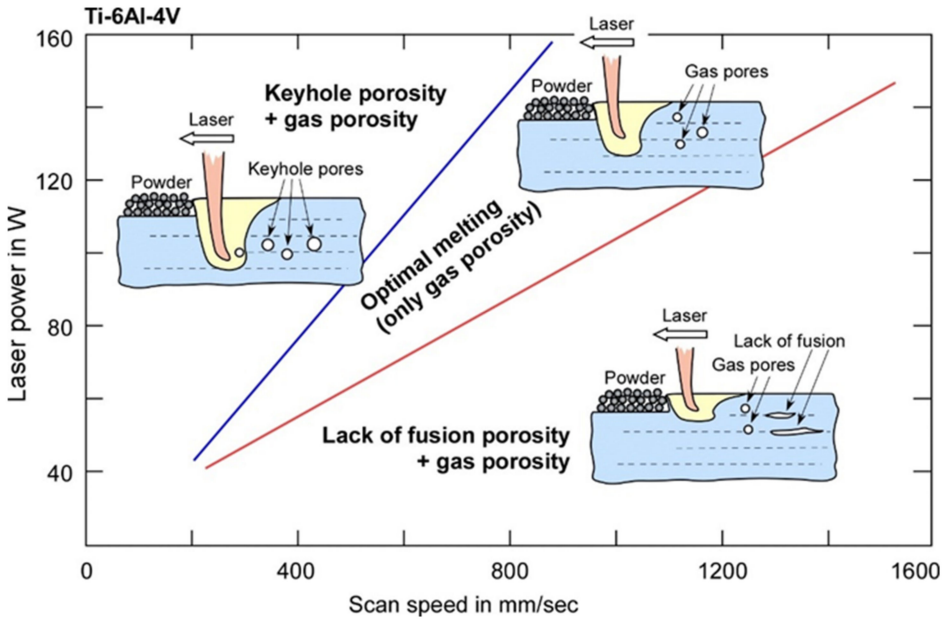


Figure 3. Overview on the formation of the different defect types as a function of laser power and scan speed, assuming that all other parameters (pattern, hatch distance, layer thickness) are kept constant; L-PBF manufactured Ti–6AL–4V; figure modified from [27]. The triangle in the middle defines the processing window.

2.4. Microcracks

A consequence of the rapid cooling in combination with the inhomogeneous temperature distribution is high internal stresses which can cause thermal cracks [21]. Note that there will be stress concentrations at non-metallic inclusions with stiffness different to the matrix material [4], which also promotes the formation of microcracks. L-PBF fabricated aluminum is prone to solidification cracking because of high thermal expansion and extended shrinkage [28]. Crack-like defects can also be surface oxide layers which are broken up and shifted to the bulk material [29].

2.5. Pronounced Surface Roughness

In the as-built condition, L-PBF parts show a much larger surface roughness than conventional parts. There are different reasons for this: one is partially melted powder at the surface due to an unstable melt pool; another is stepwise layer building, which forms "staircases", especially in overhanging structures [30] (Figure 4a). Yadollahi and Shamsaei [12], investigating a cylinder of L-PBF Inconel 718 generated in 45° direction measured a roughness of R_a ~0 µm at the upward- and R_a ~5 µm at the downward-facing surface. Relevant for fatigue, such roughness is in the order of the critical defect size discussed in Section 1.1. In Figure 4b, the notch effect of surface roughness is illustrated for L-PBF Ti–6Al–4V [31]. A roughness profile, such as the one shown in Figure 4, is not easy to measure by conventional methods because it includes undercuts (or re-entrant features). As can be seen, the stress concentration is about $K_t = 4$ or even larger. This number is in line with what is otherwise known for L-PBF [32].

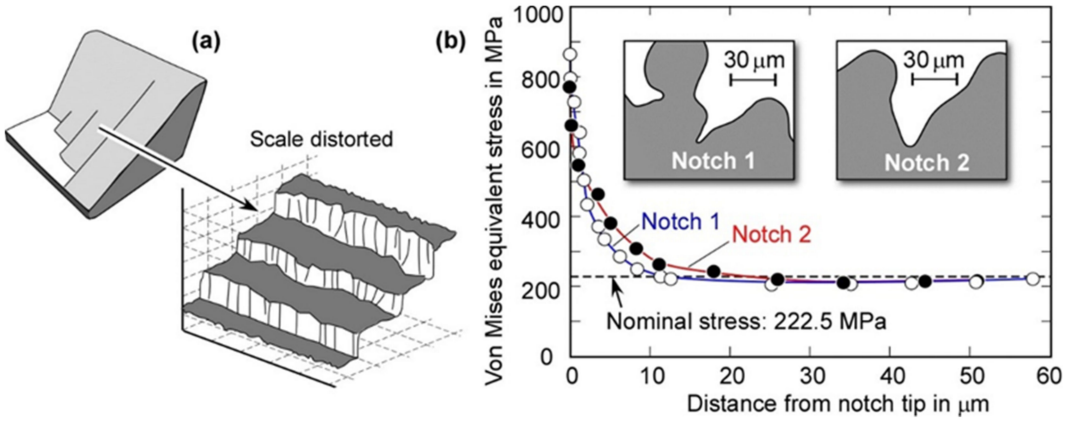


Figure 4. Surface roughness in L-PBF, as-built state: (**a**) staircase effect, according to [29], simplified; (**b**) as-built surface roughness of L-PBF Ti–6Al–4V, according to [31].

2.6. Competition between Different Defect Types

There is a competition between the different defect types: those that cause the highest stress concentration also control the fatigue behavior. Frequently, such a defect type will be surface roughness. However, when the surface is smoothed, another defect type, e.g., lack of fusion will take over this role. Note that there is the danger that sub-surface defects come to surface when the original rough surface is removed. In the as-built state the picture is further complicated by the fact that the tensile residual stress near the surface play an important role.

All the defects discussed in this section can usually be treated as cracks in the analysis [1]. This is because they are narrow enough to come close to the mechanical characteristics of cracks. Furthermore, they often emit microcracks at an early stage, which are difficult to detect but may represent a further origin of failure.

3. Determining the Fatigue Strength Taking into Account Defects

In Section 1.1, we have concluded that defects have to be taken into account in the damage assessment of additively manufactured components. Since these can be treated as cracks, fracture mechanics comes into play. In this section, three approaches will be briefly introduced.

3.1. Kitagawa–Takahashi Diagram

A traditional approach is the semi-empirical Kitagawa–Takahashi diagram (hereinafter KT diagram) [33]. The threshold cyclic stress is plotted against the crack or defect size in double-logarithmic scale, Figure 5. The diagram consists of three distinct regions. In region I, the threshold stress level $\Delta\sigma_{th}$ is defined by the plain endurance limit $\Delta\sigma_e$. Such region ends at a crack/defect size d_1 that corresponds to the critical crack size mentioned in Section 1.1 (a), at which even the largest of the microcracks arrests. Region III describes the long fatigue crack propagation regime, where crack arrest occurs when the stress intensity factor range ΔK $(= K_{max} - K_{min})$ falls below the fatigue crack propagation threshold $\Delta K_{th,LC}$. A long crack is a crack with saturated crack closure phenomenon, i.e., the crack closure is independent of the crack depth and the crack is long enough (down to a length d_2) such that the stress intensity factor concept can be applied (small-scale yielding condition). Its slope in the KT diagram is $-1/2$. Region II, between d_1 and d_2, belongs to the mechanically/physically short crack regime where both conditions are not fulfilled. The cyclic crack driving force has to be determined accounting for elastic-plastic conditions, and the crack closure phenomenon builds up gradually.

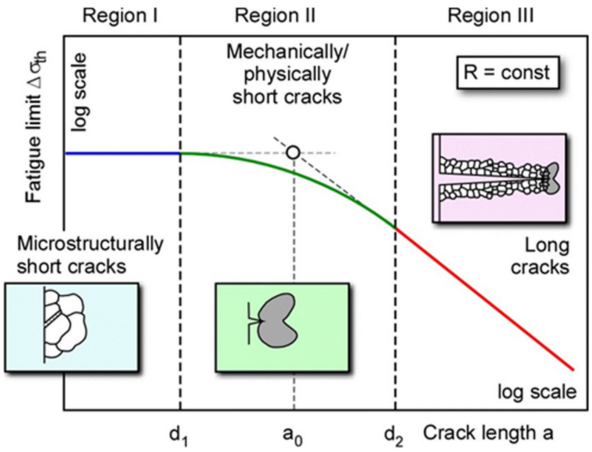


Figure 5. Schematic Kitagawa–Takahashi (KT) diagram.

Before we continue with the determination of the KT diagram, some basic explanations about the crack closure phenomenon are due. Crack closure means the premature contact of the crack faces during the unloading part of the cycle. This is important, in that crack propagation is only expected for open cracks. Different mechanisms can cause premature crack closure (Figure 6): (a) In plasticity-induced closure, the plastic zone remains in the crack wake where it causes geometrical mismatch between the crack faces. (b) Roughness-induced crack closure is the consequence of crack face asperity, amplified by effects such as crack kinking and branching. (c) Oxide-induced closure occurs in materials prone to corrosion—the crack faces are covered by a thin oxide layer, which is removed locally by crack face friction at low mean stresses. At these sites, the material oxidizes again. In this way, an oxide debris layer is formed that is much thicker than the initial layer. (d) Some materials, e.g., some austenitic steels, tend to undergo strain-induced phase transformation in the highly stretched region at the crack tip. This phenomenon is accompanied by a volume expansion of about 5%, which generates compressive stresses at the crack tip; see [34].

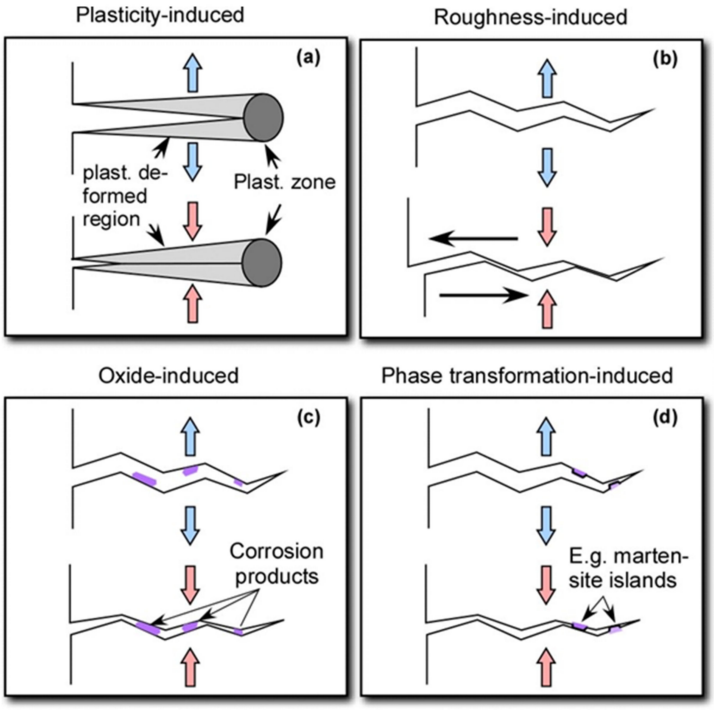


Figure 6. Crack closure mechanisms: (**a**) plasticity-induced; (**b**) roughness-induced; (**c**) oxide-induced; (**d**) phase transformation-induced.

A common parameter for the characterization of crack closure is the closure parameter $U = \Delta K_{eff}/\Delta K$ with the effective cyclic stress intensity factor ΔK_{eff} being the part of ΔK over which the crack is open. At the stage of the physically short crack growth, the closure effect does not initially exist because it presupposes a certain extension of the crack wake, i.e., $U = 1$. It then gradually builds up and U decreases with crack extension Δa until it reaches a crack size independent value when the crack enters the stage of long crack growth; these mechanisms are explained in Figure 7.

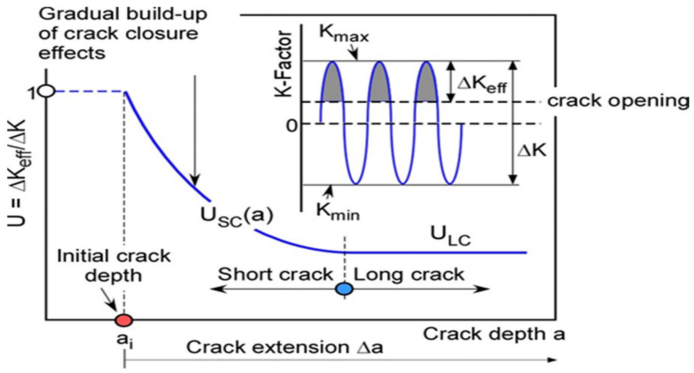


Figure 7. Development of the crack closure phenomenon at the physically short crack propagation stage; schematic view.

Note that the crack growth is not only influenced by effects acting at the crack wake but also by factors that affect the conditions ahead of the crack tip. For example, crack branching can cause mechanical shielding of the two crack tips and martensite formation is combined with type II residual stress (intergranular), which will influence the crack driving force and perhaps crack branching (see the discussion in [34].

The KT diagram can be determined in different ways: (a) empirically by the determination of the endurance limit on specimens with narrow artificial notches; (b) by the El Haddad approach [35]; and (c) theoretically from the cyclic R curve, which will be presented in Section 3.3. The most common method is (b). Applying this, the diagram is obtained by

$$\Delta\sigma_{th} = \Delta K_{th,LC}/\sqrt{\pi(a + a_0)} \quad (1)$$

The parameter a_0 is the so-called El Haddad parameter, which provides an estimate of the transition between short and long crack regime in region II. It can be determined in reverse by Equation (1) when the long fatigue crack propagation threshold $\Delta K_{th,LC}$ and the plain endurance limit of the material, $\Delta\sigma_{th} = \Delta\sigma_e$, are used. Two problems are faced: For materials prone to corrosion, the value of $\Delta K_{th,LC}$ can depend on the method of experimental determination at low R ratios ($= K_{min}/K_{max}$) [36], and the shape of the curve is predetermined by the equation. As will be shown in Section 3.3, another shape is obtained in region II when the KT diagram is determined by the cyclic R curve analysis.

Figure 8 provides two examples of KT diagrams obtained for L-PBF manufactured AlSi10Mg and Ti-6Al-4V [37]. They are based on literature data. Note that the crack size a is replaced by the Murakami's parameter $\sqrt{area}$ on the abscissa; see Section 3.2.

The basic advantage of the KT diagram for characterizing the fatigue behavior of L-PBF fabricated materials is that the defect size does not have to be known in advance. Instead, the threshold stress level is determined as a function of the crack or defect size. Depending on the design requirements, specifications for non-destructive testing (NDT) can be provided this way, which makes the KT diagram a simple and powerful tool for the qualification of AM parts.

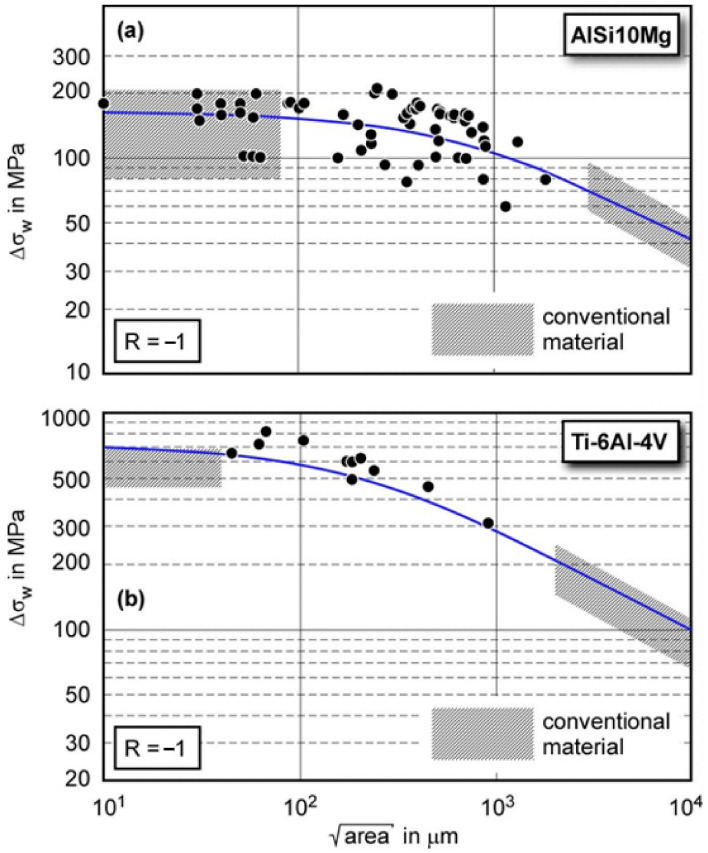


Figure 8. KT diagrams based on literature data for (**a**) L-PBF AlSi10Mg and (**b**) L-PBF Ti-6Al-4V [37]. The term $\Delta\sigma_w$ designates the endurance limit $\Delta\sigma_e$ at $R = -1$. The blue solid curves have been obtained by the El Haddad approach (Equation (1)).

3.2. Murakami's $\sqrt{area}$ Approach

This approach [1] is based on a number of empirical observations. First, Murakami found that the maximum K factor along the front of small cracks, $K_{I,max}$, could be approximated by the projected area of the crack, *area*, within an accuracy of 10% by

$$K_{I,max} \approx 0.65 \cdot \sigma \cdot \sqrt{\pi\sqrt{area}} \tag{2}$$

The parameter $\sqrt{area}$ was then used to provide correlations with the fatigue crack propagation threshold ΔK_{th} and the threshold stress level $\Delta\sigma_{th}$. For the latter, a solution was found as

$$\Delta\sigma_{th} = 2.86 \cdot (HV + 120) \cdot \left(\sqrt{area}\right)^{-1/6} \cdot [(1 - R)/2]^{\alpha} \tag{3}$$

which can be interpreted as a modification of the equation in Figure 1 considering the nonlinear curve sections. The exponent α is given by $0.226 + HV \cdot 10^{-4}$. Equation (3) refers to surface cracks, and for embedded cracks, the coefficient 2.86 must be replaced by 3.12. Note that Equation (3) is applied to cracks as well as defects such as pores or surface roughness. Its validity is restricted to region II of the KT diagram. The units in Equation (3) are MPa for $\Delta\sigma_{th}$ and µm for $\sqrt{area}$.

3.3. Cyclic R Curve Approach

Figure 9 shows a so-called cyclic R curve which describes the dependence of the fatigue crack propagation threshold ΔK_{th} on the fatigue crack extension Δa in the physically short crack regime. A discussion of the experimental determination of this curve is provided

in [38]. Note that the threshold consists of two components, an intrinsic (or closure free) one, $\Delta K_{th,eff}$, and a closure related one, ΔK_{op} such that

$$\Delta K_{th} = \Delta K_{th,eff} + \Delta K_{th,op} \quad (4)$$

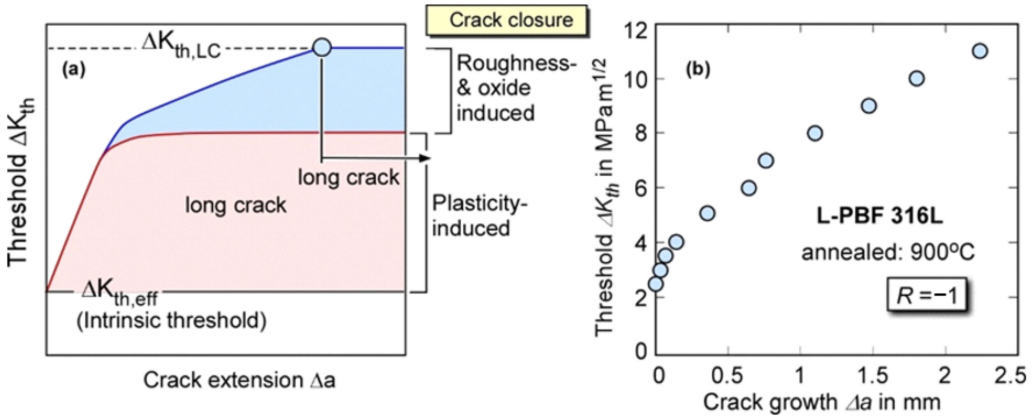


Figure 9. Cyclic R curve: (**a**) schematic view, including the effect of the crack closure effects on $\Delta K_{th,op}$; (**b**) example of a curve for L-PBF steel 316L (Werner, T., BAM Berlin, 2020).

While $\Delta K_{th,eff}$ is a material parameter that only depends on the elastic constants of the material and its lattice type [39], $\Delta K_{th,op}$ is characteristic for the material, e.g., its grain size (via the roughness-induced closure effect), the stress ratio R, and for physically short cracks, the crack extension Δa. The intrinsic threshold is in the order of 2.4–2.6 MPa $m^{1/2}$ for steels, 0.9–1.9 MPa $m^{1/2}$ for aluminum alloys, and 1.7–2.5 MPa $m^{1/2}$ for titanium alloys [40].

The principle of a cyclic R curve analysis is illustrated in Figure 10. Cyclic crack driving force curves of the component are plotted as functions of the crack depth ($\Delta K_p - a$) for three stress levels $\Delta\sigma_1$ to $\Delta\sigma_3$. As mentioned above, an elastic-plastic parameter has to be used as crack driving force. This is indicated by the index "p" in ΔK_p, which is a plasticity-corrected ΔK formally derived from the J-integral [41,42]. The cyclic R curve is also plotted in Figure 10. Its origin is given by the intrinsic threshold, $\Delta K_{th,eff}$, on the ordinate and by an initial crack depth a_i on the abscissa.

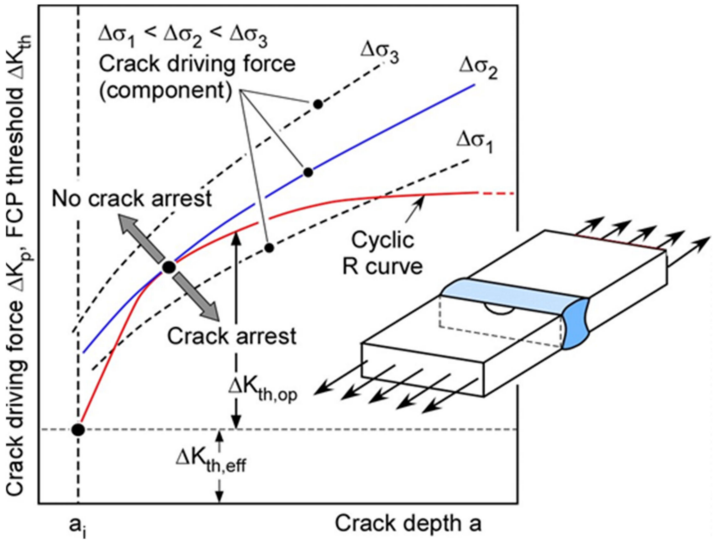


Figure 10. Principle of a cyclic R curve analysis to determine the fatigue limit based on crack arrest.

If a_i is known, the fatigue limit of a component can be obtained by the crack driving force curve, which tangentially touches the R curve (in the example $\Delta\sigma_2$). Zerbst and Madia have developed a method for determining a_i using a crack arrest approach [7,43];

for alternative methods, see [44]. When applied in the frame of a KT diagram approach, a_i does not have to be specified but is simply chosen as an input parameter.

The cyclic R curve in conjunction with the crack driving force in the component ΔK_p can also be used for the simulation of fatigue crack propagation in the mechanically/physically short and the subsequent long fatigue propagation regime. Combined with a failure criterion, the cyclic R curve can also be used for the prediction of the finite life branch of the S–N curve. The methodology is described in detail in [43,45]. Application to L-PBF 316L is shown in Figure 11. It contains two approaches, the IBESS method of the authors and a similar approach of Chapetti in a slightly modified version according to [46].

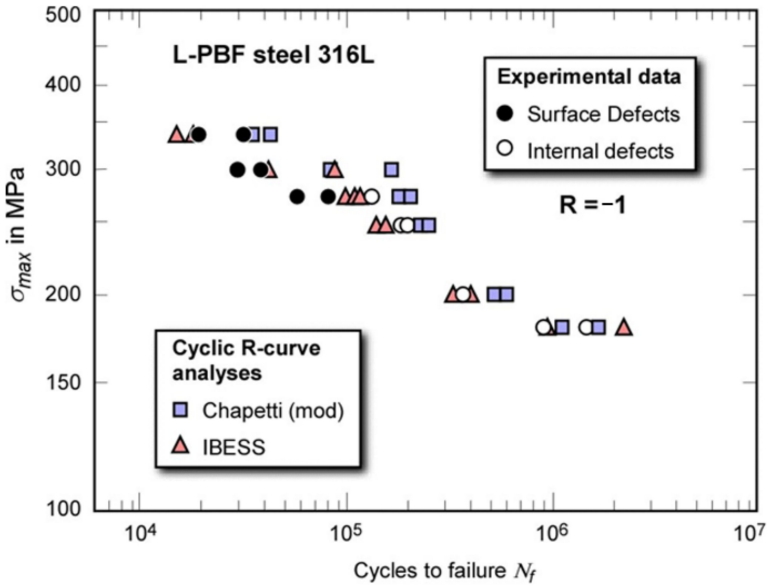


Figure 11. Application of cyclic R curve analyses to the determination of S–N curve data of L-PBF steel 316L according to [47].

When the KT diagram is determined by crack arrest analysis using a cyclic R curve approach, the curve lies below the one predicted by the El Haddad approach. This is shown in Figure 12. Consequently, the predicted threshold stress level in region II is smaller if one uses the cyclic R curve approach than in the case of the conventional (KT) and El Haddad approaches (see, e.g., the discussion in [14,47,48]). The explanation of this discrepancy is a subject of ongoing research. It is certainly of high importance for the KT concept, since the difference can be in the order of 20% or more. The potential of the determination of the KT diagram by a cyclic R curve analysis is that a component-based KT diagram can be obtained.

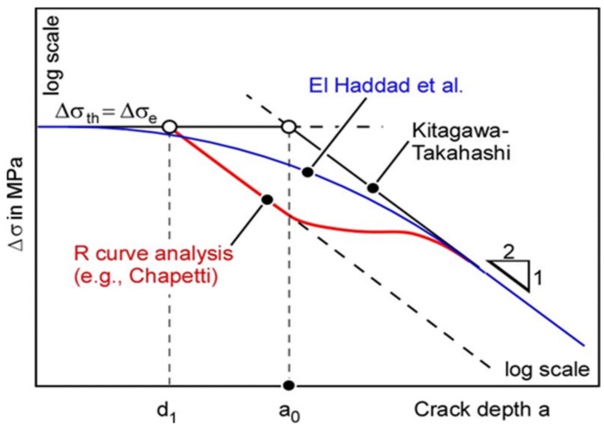


Figure 12. Schematic view of the discrepancy between the conventionally and by means of cyclic R curve analysis obtained KT diagram.

A point has to be added: For stress levels above the endurance limit, multiple crack propagation can occur. The determination of the KT diagram for this can also be made by cyclic R curve analysis, though in a statistical manner. The reader may refer to [43,45] for further details.

4. Representative Material Properties

One of the major issues in the applicability of damage tolerance to AM parts is related to the use of material properties representative of the material behavior in damage-critical locations; see Section 5. As mentioned before, it has been shown that the microstructure in L-PBF metals can locally vary (see [43,49,50]). To tackle this problem, two possible routes are possible: (i) derive material properties on small-scale specimens extracted from the component in those specific locations taken into account in the fatigue assessment; (ii) fabricate specimens characterized by the very same microstructure of the regions of interest in the component (identical thermal history). The principle is known from welds, where samples made of pure HAZ material can be produced. It is crucial that the samples must experience the same thermal conditions and, in particular, the same cooling rate as the HAZ in the component. This principle can be transferred to L-PBF fabricated material, but due to the influence of a great number of technological parameters, the situation is far more complicated than with welds. The general scheme is illustrated in Figure 13.

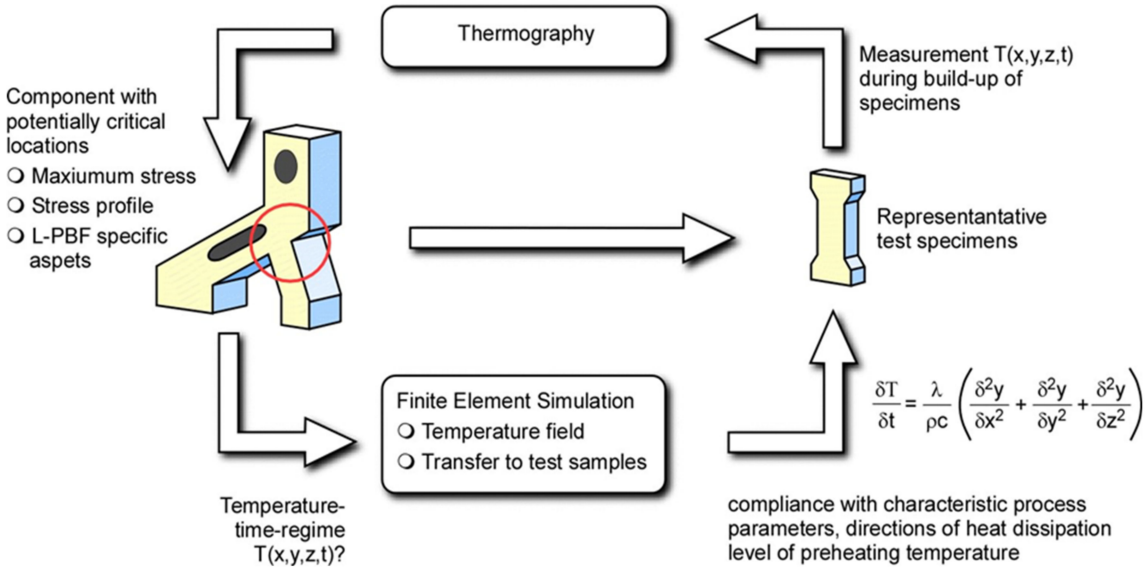


Figure 13. Principle of the fabrication of representative test specimens for the damage critical locations in an L-PBF component.

The transfer of a temperature history to a specimen makes it first necessary to determine this history for the critical area of a component. The heat conduction in already built structures and the substrate plate is of particularly high importance. It was shown that geometrical features obstructing this heat flow lead to significant heat accumulation [11]. Here, a temperature field calculation by means of FEM presents a suitable option. A process strategy needs then to be derived which replicates the calculated temperature history during build-up of the specimen. The following points must be taken into account:

(a) Maintaining the main process parameters which determine the energy input, e.g., laser power, scanning speed, layer thickness, hatch pattern and distance;
(b) Maintaining the build-up orientation;
(c) Using an interlayer time that would occur in the production of the component;
(d) Considering the heat accumulation previously built up in the component, which might be transferred to the specimen by accordingly adjusted preheating temperature or the build-up of a base structure.

Finally, thermography can be used to validate this approach by comparing the surface temperatures during build-up of the specimens and the component. It is clear that such an approach will not be applicable for arbitrary geometries. In particular, the transfer of a temperature field of small, narrow features to a larger sample is subject to restrictions. However, this promising approach is the subject of ongoing research activities.

5. Identification of Potentially Critical Sites

It has already been mentioned in Section 1.3 that the selection of the potentially damage-relevant locations in a L-PBF component are not simply given by the highest stress. In addition, aspects relevant to L-PBF must be taken into account. One of them is certainly the building direction (relative to the local loading direction, i.e., the principal stress direction), but other factors such as inhomogeneous roughness or defect spatial distribution may also be important. When local yielding is expected to play a role, local stiffness is important as a classification criterion. Gorelik has coined the term "zone-based approach" [51]. The assessment should concentrate on zones at which the following features are similar: (a) material properties (microstructure, material parameters, defect distribution), (b) geometry (e.g., thin wall sections), (c) feasibility for non-destructive tests, and (d) post-fabrication treatment. We can add that residual stress should also be comparable.

Here, the following procedure is proposed:

(a) Potentially critical locations in the component should be identified by means of finite element analysis. The choice of the sites to be considered could be driven by the stress value (as a certain percentage of the yield strength, e.g., 50%).

(b) The pre-selected positions are classified according to certain criteria: geometrical features (e.g., thin wall sections having distinct local stiffness and/or plasticity effects), the build orientation with respect to the loading direction, and possible defect clusters. With respect to the residual stress, it is recommended to relieve it using suitable post-fabrication treatment. If it is possible to determine RS, it may also form a classification criterion.

(c) All sites identified under (a) shall be grouped into the classes of (b).

For each class or category, the stress profiles in the wall thickness direction are determined. This may require finite element mesh refinement, e.g., realized by the sub-model technique. As a result, one or sometimes two cases per category are identified, which show the highest stresses (peak value and distribution). Only these will then serve as a basis for further analysis.

The further steps have already been described in the previous sections. For the one or two finally selected cases in each category, the thermal history is reconstructed, and specimens are prepared under similar manufacturing conditions. These specimens are then used to determine the material parameters needed for further analysis. Such parameters depend on the model used. In the simplest case, the model is the S–N curve and the main parameter the endurance limit. For KT and cyclic R curve applications, the data of the $da/dN - \Delta K$ curve, including the long fatigue crack propagation threshold $\Delta K_{th,LC}$, are needed. Finally, the cyclic R curve approach requires the cyclic R curve.

Note that a fracture mechanics-based assessment should consider the following aspects:

The surface roughness will usually not be reproduced in the specimens, but it can be regarded as a defect-like feature (initial crack depth);

Essential input variables such as defects and material properties usually show large scatter, which is inherent to the AM process. Therefore, a probabilistic fatigue assessment is suggested in which fatigue lives can be calculated for given target failure probabilities.

6. Summary

A concept is presented for the damage-tolerant design of metallic components made by additive manufacturing, especially by means of laser powder bed fusion. This takes into account the specific aspects of this class of applications. The challenges include the big

role of material defects and the pronounced inhomogeneity of the material properties at different positions of the component. Not discussed is the consideration of residual stresses. Instead, their elimination is required as a realistic scenario for the current state-of-the-art.

The main elements of the present concept are (a) the identification of the critical location(s) in the component on the basis of a classification system which, in addition to the local stresses, considers other items such as local stiffness and AM-specific aspects, e.g., the build orientation; (b) manufacturing of representative specimens based on thermal simulation; (c) the application of fracture mechanics approaches for short crack propagation and crack arrest, with the aim of establishing the maximum permissible load as a function of defect size. This can then be used as input information for non-destructive testing or, if the distribution of the defect sizes is known, for the determination of the failure load.

Author Contributions: Conceptualization, U.Z. and M.M.; methodology, U.Z. and M.M.; formal analysis, U.Z. and M.M.; investigation, U.Z. and M.M.; data curation, U.Z. and M.M.; writing—original draft preparation, U.Z. and M.M.; writing—review and editing, U.Z., M.M., K.H. and G.B.; visualization, U.Z.; supervision, U.Z.; project administration, U.Z. and G.B.; funding acquisition, U.Z. and G.B. All authors have read and agreed to the published version of the manuscript.

Funding: No external funding.

Informed Consent Statement: Not necessary.

Data Availability Statement: Not applicable.

Conflicts of Interest: The authors declare no conflict of interest.

Nomenclature

a	crack length (crack depth for surface cracks)
a_i	initial crack depth for fracture mechanics analysis
a_0	fit parameter of the El Haddad approach
c	specific heat capacity
d_1, d_2	length scales (crack depth) in the Kitagawa–Takahashi diagram
da/dN	crack propagation rate
HV	Vickers hardness
K_{max}	maximum K-factor in a loading cycle
K_{min}	minimum K-factor in a loading cycle
K_{op}	K-factor above which the crack is open
K_t	stress concentration factor
$K_{I,max}$	maximum K factor along the front of a small crack
N	number of loading cycles
R	loading ratio ($=\sigma_{min}/\sigma_{max}$ or K_{min}/K_{max})
R_a	surface roughness parameter
R_m	ultimate tensile strength
t	time
T	temperature
U	crack closure parameter ($\Delta K_{eff}/\Delta K$)
U_{LC}	crack closure parameter for long cracks
U_{SC}	crack closure parameter for short cracks
x, y, z	coordinates in longitudinal, transverse and thickness direction
Δa	crack extension
ΔK	K-factor range (K_{max}–K_{min}), cyclic K-factor
ΔK_{eff}	effective K-factor range ($=K_{max}$–K_{op})
ΔK_p	plasticity corrected K-factor range
$\Delta K_{th,eff}$	intrinsic fatigue crack propagation threshold (no crack closure effect)
$\Delta K_{th,LC}$	fatigue crack propagation threshold in the long crack regime
$\Delta K_{th,op}$	part of ΔK_{th} due to the crack closure phenomenon

$\Delta\sigma$	stress range (σ_{max}–σ_{min})
$\Delta\sigma_e$	endurance limit based on stress range
$\Delta\sigma_{th}$	threshold stress (dependence of the endurance limit on defect size)
λ	thermal conductivity
ρ	density
σ_e	endurance limit based on stress amplitude
σ_w	σ_e for $R = -1$
$\sqrt{area}$	square root of defect (or crack) area normal to the loading direction;

Abbreviations

AM	additive manufacturing
IBESS	Method for fracture mechanics prediction of the fatigue strength (originally developed for weldments; the acronym stands for the German translation of "Integral fracture mechanics determination of the fatigue strengths of weldments")
KT	Kitagawa–Takahashi diagram
L-PBF	laser powder bed fusion (formerly SLM)
NDT	non-destructive testing
S–N curve	stress (amplitude) versus number of loading cycles to failure.

References

1. Murakami, Y. *Metal Fatigue. Effects of Small Defects and Nonmetallic Inclusions*; Elsevier: Oxford, UK, 2002.
2. Zerbst, U.; Madia, M.; Klinger, C.; Bettge, D.; Murakami, Y. Defects as the root cause of fatigue failure of metallic components. Part I: Basic aspects. *Eng. Fail. Anal.* **2019**, *97*, 777–792. [CrossRef]
3. Zerbst, U.; Madia, M.; Klinger, C.; Bettge, D.; Murakami, Y. Defects as the root cause of fatigue failure of metallic components. Part II: Non-metallic inclusions. *Eng. Fail. Anal.* **2019**, *98*, 228–239. [CrossRef]
4. Zerbst, U.; Madia, M.; Klinger, C.; Bettge, D.; Murakami, Y. Defects as the root cause of fatigue failure of metallic components. Part III: Cavities, dents, corrosion pits, scratches. *Eng. Fail. Anal.* **2019**, *97*, 759–776. [CrossRef]
5. Miller, K.J. The two thresholds of fatigue behavior. *Fatigue Fract. Eng. Mat. Struct.* **1993**, *16*, 931–939. [CrossRef]
6. Yamashita, Y.; Murakami, T.; Mihara, R.; Okada, M.; Murakami, Y. Defect analysis and fatigue design basis for Ni-based superalloy 718 manufactured by selective laser melting. *Int. J. Fatigue* **2018**, *117*, 485–495. [CrossRef]
7. Zerbst, U.; Madia, M.; Vormwald, M.; Beier, H.T. Fatigue strength and fracture mechanics—A general perspective. *Eng. Fract. Mech.* **2018**, *198*, 2–23. [CrossRef]
8. Murakami, Y.; Masuo, H.; Tanaka, Y.; Nakatani, M. Defect analysis for additively manufactured materials in fatigue from a viewpoint of quality control and statistics of extremes. *Procedia Struct. Integr.* **2019**, *19*, 113–122. [CrossRef]
9. Gu, D.; Hagedorn, Y.-C.; Meiners, W.; Meng, G.; Batista, R.J.S.; Wissenbach, K.; Poprawe, R. Densification behavior, microstructure evolution, and wear performance of selective laser melting processed commercially pure titanium. *Acta Mater.* **2012**, *60*, 3849–3860. [CrossRef]
10. Mohr, G.; Altenburg, S.J.; Hilgenberg, K. Effects of inter layer time and build height on resulting properties of 316L stainless steel processed by laser powder bed fusion. *Addit. Manuf.* **2020**, *32*, 101080. [CrossRef]
11. Mohr, G.; Scheuschner, N.M.; Hilgenberg, K. In situ heat accumulation by geometrical features obstructing heat flux and by reduced inter layer times in laser powder bed fusion of AISI 316L stainless steel. *Procedia CIRP* **2020**, *94*, 155–160. [CrossRef]
12. Yadollahi, A.; Shamsaei, N. Additive manufacturing of fatigue resistant materials: Challenges and opportunities. *Int. J. Fatigue* **2017**, *98*, 14–31. [CrossRef]
13. Zhang, M.; Sun, C.-N.; Zhang, X.; Goh, P.C.; Wei, J.; Li, H.; Hardacre, D. Elucidating the relations between monotonic and fatigue properties of laser powder bed fusion stainless steel 316L. *JOM* **2018**, *70*, 390–395. [CrossRef]
14. Zerbst, U.; Bruno, G.; Buffiere, J.-Y.; Wegener, T.; Niendorf, T.; Wu, T.; Zhang, X.; Kashaev, N.; Meneghetti, G.; Hrabe, N.; et al. Damage tolerant design of additively manufactured metallic components subjected to cyclic loading: State of the art and challenges. *Prog. Mat. Sci.* **2021**. in print. [CrossRef]
15. Mishurova, T.; Artzt, K.; Haubrich, J.; Requena, G.; Bruno, G. New aspects about the research for the most relevant parameters optimizing SLM materials. *Addit. Manuf.* **2019**, *25*, 325–334.
16. Mishurova, T.; Cabeza, S.; Thiede, T.; Nadammal, N.; Kromm, A.; Klaus, M.; Genzel, C.; Haberland, C.; Bruno, G. The influence of the support structure on residual stress and distortion in SLM Inconel 718 parts. *Metall. Mater. Trans. A* **2018**, *49*, 3038–3046. [CrossRef]
17. Mishurova, T.; Artzt, K.; Haubrich, J.; Requena, G.; Bruno, G. Exploring the correlation between subsurface residual stresses and manufacturing parameters in Laser Powder Bed Fused Ti-6Al-4V. *Metals* **2019**, *9*, 261. [CrossRef]
18. Mishurova, T.; Artzt, K.; Rehmer, B.; Haubrich, J.; Ávila, L.; Schoenstein, F.; Serrano-Munoz, I.; Requena, G.; Bruno, G. Separation of the impact of residual stress and microstructure on the mechanical performance of LPBF Ti-6Al-4V at elevated temperature. *Int. J. Fatigue* **2021**. under review. [CrossRef]

19. Gumpinger, J.; Brandão, A.D.; Beevers, E.; Rohr, T.; Ghidini, T.; Beretta, S.; Romano, S. Expression of additive manufacturing surfaced irregularities through a flaw-based assessment. In Proceedings of the ASTM Symposium on Structural Integrity of Additive Manufactured Parts, Washington, DC, USA, 6–8 November 2018; ASTM International: West Conshohocken, PA, USA, 2018.
20. Beretta, S.; Gargourimotlagh, M.; Folletti, S.; Rigoni, L.; Riccio, M. Fatigue strength assessment and surface rating for "as built" AlSi10Mg manufactured by SLM with different build directions. *Int. J. Fatigue* **2021**, *139*, 105737.
21. Zhang, B.; Li, Y.; Bai, Q. Defect formation mechanisms in selective laser melting: A review. *Chin. J. Mech. Eng.* **2017**, *30*, 515–527. [CrossRef]
22. Tammas-Williams, S.; Zhao, H.; Leonard, F.; Derguti, F.; Todd, I.; Prangnell, P.B. XCT analysis of their influence of melt strategies on defect population in Ti-6Al-4V components manufactured by Selective Electron Beam Melting. *Mater. Charact.* **2015**, *102*, 47–61. [CrossRef]
23. Laquai, R.; Müller, B.R.; Kasperovich, G.; Haubrich, J.; Requena, G.; Bruno, G. X-ray refraction distinguishes unprocessed powder from empty pores in selective laser melting Ti-6Al-4V. *Mater. Res. Lett.* **2018**, *6*, 130–135. [CrossRef]
24. Laquai, R.; Müller, B.R.; Kasperovich, G.; Requena, G.; Haubrich, J.; Bruno, G. Classification of defect types in SLM Ti-6Al-4V by x-ray refraction topography. *Mater. Perform. Charact.* **2020**, *9*, 82–93.
25. Laquai, R.; Müller, B.R.; Schneider, J.A.; Kupsch, A.; Bruno, G. Using SXRR to probe the nature of discontinuities in SLM Additive Manufactured Inconel 718 specimens. *Metall. Mater. Trans. A* **2020**, *51A*, 4146–4157. [CrossRef]
26. Agarwala, M.; Bourell, D.; Beaman, J.; Marcus, H.; Barlow, J. Direct selective laser sintering of metals. *Rapid Prototyp. J.* **1995**, *1*, 26–36. [CrossRef]
27. Cao, X.; Wallace, W.; Immarigeon, J.-P.; Poon, C. Research and progress in laser welding of wrought aluminum alloys. II. Metallurgical microstructures, defects and mechanical properties. *Mater. Manuf. Process.* **2002**, *18*, 23–49. [CrossRef]
28. Gong, H.; Rafi, K.; Gu, H.; Starr, T.; Stucker, B. Analysis of defect generation in Ti6Al-4V parts made using powder bed fusion additive manufacturing processes. *Addit. Manuf.* **2014**, *1*, 87–98.
29. Olakanmi, E.O.; Cochrane, R.F.; Dalgarno, K.W. A review on selective laser sintering/melting (SLS/SLM) of aluminium alloy powders: Processing, microstructure, and properties. *Prog. Mater. Sci.* **2015**, *74*, 401–477. [CrossRef]
30. Sikder, S.; Barani, A.; Kishawy, H.A. Effect of adaptive slicing on surface integrity in additive manufacturing. In Proceedings of the ASME 2014 International Design Engineering Technical Conferences and Computers and Information in Engineering Conference, Buffalo, NY, USA, 17–20 August 2014.
31. Vayssette, B.; Saintier, N.; Brugger, C.; El May, M.; Pessard, E. Numerical modelling of surface roughness effect on the fatigue behaviour of Ti-6Al-4V obtained by additive manufacturing. *Int. J. Fatigue* **2019**, *123*, 180–195. [CrossRef]
32. Kahlin, M.; Ansell, H.; Moverare, J.J. Fatigue behaviour of notched additive manufactured Ti6Al4V with as-build surfaces. *Int. J. Fatigue* **2017**, *101*, 51–60. [CrossRef]
33. Kitagawa, H.; Takahashi, S. Applicability of fracture mechanics to very small cracks or the cracks in the early stage. In Proceedings of the Second International Conference on Mechanical Behavior of Materials, Boston, MA, USA, 16–20 August 1976; pp. 627–631.
34. Werner, T.; Madia, M.; Zerbst, U. Damage tolerant design of additively manufactured metallic components. *Int. J. Fatigue* **2021**. submitted.
35. Haddad, M.H.; Smith, K.N.; Topper, T.H. Fatigue crack propagation of short cracks. *J. Eng. Mater. Technol.* **1979**, *101*, 42–46. [CrossRef]
36. Zerbst, U.; Vormwald, M.; Pippan, R.; Gänser, H.-P.; Sarrazin-Baudoux, C.; Madia, M. About the fatigue crack propagation threshold of metals as a design criterion—A review. *Eng. Fract. Mech.* **2016**, *153*, 190–243. [CrossRef]
37. Beretta, S.; Romano, S. A comparison of fatigue strength sensitivity to defects for materials manufactured by AM or traditional processes. *Int. J. Fatigue* **2017**, *94*, 178–191. [CrossRef]
38. Maierhofer, J.; Kolitsch, S.; Pippan, R.; Gänser, H.-P.; Madia, M.; Zerbst, U. The cyclic R-curve—Determination, problems, limitations and application. *Eng. Fract. Mech.* **2018**, *198*, 45–64. [CrossRef]
39. Pokluda, J.; Pippan, R.; Vojtek, T.; Hohenwarter, A. Near-threshold behavior of shear-mode fatigue cracks in metallic materials. *Fatigue Fract. Eng. Mater. Struct.* **2014**, *37*, 232–254. [CrossRef]
40. Hadrboletz, A.; Weiss, B.; Stickler, R. Fatigue threshold of metallic materials—A review. In *Handbook of Fatigue Crack Propagation in Metallic Structures*; Carpinteri, A., Ed.; Elsevier: Amsterdam, The Netherlands, 1994; pp. 847–882.
41. Zerbst, U.; Madia, M.; Hellmann, D. An analytical fracture mechanics model for estimating of S-N curves of metallic alloys containing large second phase particles. *Eng. Fract. Mech.* **2012**, *82*, 115–134. [CrossRef]
42. Madia, M.; Thoffo Ngoula, D.; Zerbst, U.; Beier, H.T. Approximation of the crack driving force for cracks at notches under static and cyclic loading. *Procedia Struct. Integr.* **2017**, *5*, 875–882. [CrossRef]
43. Zerbst, U.; Madia, M.; Schork, B.; Hensel, J.; Kucharczyk, P.; Tchoffo Ngoula, D.; Tchuindjang, D.; Bernhard, J.; Beckmann, C. Fatigue and fracture of weldments. In *The IBESS Approach for the Determination of the Fatigue Life and Strength of Weldments by Fracture Mechanics Analysis*; Springer Nature Switzerland AG: Cham, Switzerland, 2019.
44. Zerbst, U.; Madia, M.; Vormwald, M. Applying fracture mechanics to fatigue strength determination—Some basic considerations. *Eng. Fract. Mech.* **2019**, *126*, 188–201. [CrossRef]
45. Madia, M.; Zerbst, U.; Beier, H.T.; Schork, B. The IBESS model—Elements, realisation and validation. *Eng. Fract. Mech.* **2018**, *198*, 171–208. [CrossRef]

46. Chapetti, M.D.; Guerrero, A.O. Estimation of notch sensitivity and size effect on fatigue resistance. *Procedia Eng.* **2013**, *66*, 323–333. [CrossRef]
47. Bergant, M.A.; Werner, T.; Madia, M.; Yawny, A.A.; Zerbst, U. Applying short crack propagation analysis to fatigue strength assessment of additively manufactured materials: An application to AISI 316L. *Int. J. Fatigue* **2021**, submitted.
48. Garb, C.; Leitner, M.; Stauder, B.; Schnubel, D.; Grün, F. Application of modified Kitagawa-Takahashi diagram for fatigue strength assessment of cast Al-Si-Cu alloys. *Int. J. Fatigue* **2018**, *111*, 256–265. [CrossRef]
49. Nadammal, N.; Cabeza, S.; Mishurova, T.; Thiede, T.; Kromm, A.; Seyfert, C.; Farahbod, L.; Haberland, C.; Schneider, J.A.; Dolabella Portella, P.; et al. Effect of hatch length on the development of microstructure texture and residual stresses in selective laser melted superalloy Inconel 718. *Mater. Des.* **2017**, *134*, 139–150. [CrossRef]
50. Serrano-Munoz, I.; Mishurova, T.; Thiede, T.; Sprengel, M.; Nadammal, N.; Nolze, G.; Saliwan-Neumann, R.; Evans, A.; Bruno, G. The residual stress in as-built Laser Powder Bed Fusion IN718 alloy as a consequence of the microstructure induced by the scan strategy. *Sci. Rep.* **2020**, *10*, 14645. [CrossRef]
51. Gorelik, M. Additive manufacturing in the context of structural integrity. *Int. J. Fatigue* **2017**, *94*, 168–177. [CrossRef]